

Fabrication of PMMA micro- and nanofluidic channels by proton beam writing: electrokinetic and morphological characterization

Kambiz Ansari Mahabadi¹, Isabel Rodriguez²,
Sow Chorng Haur³, Jeroen Anton van Kan¹,
Andrew Anthony Bettiol¹ and Frank Watt¹

¹ Center for Ion Beam Applications, Physics Department, National University of Singapore,

2 Science Drive 3, Singapore 117542

² Institute of Material Research and Engineering, 3 Research Link, Singapore 117602

³ Physics Department, National University of Singapore, Singapore 117542

E-mail: phyamk@nus.edu.sg

Received 6 February 2006, in final form 30 March 2006

Published 28 April 2006

Online at stacks.iop.org/JMM/16/1170

Abstract

The fabrication of microfluidic channels in poly(methylmethacrylate) (PMMA) by proton beam writing and the characterization of their electrokinetic behavior are reported. Microchannels down to 200 nm width have been fabricated in high-molecular-weight, thick PMMA sheets and a surface smoothness of 2.45 nm for the sidewalls of the channels was measured using atomic force microscopy. The polymeric channels were sealed using thermal bonding. The methods of digital video microscopy and current monitoring were used for characterization of the electrokinetic phenomena. The electrokinetic properties of the PMMA rectangular microchannels were measured in 20 mM buffered solutions of phosphate (pH 7.20), tris (pH 8.00) and borate (pH 9.05) at different voltages. In addition, particle image velocimetry was used to determine the electroosmotic flow profile and the electrophoretic mobility of 600 nm polystyrene microspheres. A theoretical model was developed to predict the bulk electroosmotic flow of phosphate buffer solution in the PMMA microchannels and this model showed good agreement with the measured electroosmotic mobilities.

Nomenclature

		ρ	density of the fluid (kg m^{-3})
		H	channel height
		k_B	Boltzmann constant ($\text{J mol}^{-1} \text{K}^{-1}$)
ψ	potential field (V)	L	channel length (m)
E	electric field (V m^{-1})	μ	mobility ($\mu\text{m}^2 \text{V}^{-1} \text{s}^{-1}$)
ε	electrical permittivity of the solution ($\text{C V}^{-1} \text{m}^{-1}$)	n_0	bulk concentration of ions (m^{-3})
EDL	electric double layer	P	hydraulic pressure in the x -direction (Pa)
η	dynamic or absolute viscosity of the fluid (N s m^{-2})	Re	Reynolds number
ν	kinematic viscosity, dynamic viscosity/density ($\text{m}^2 \text{s}^{-1}$)	T	temperature
ρ_e	net charge density (C m^{-3})	$U(u, v, w)$	fluid velocity with components in x , y and z flow directions respectively ($\mu\text{m s}^{-1}$)

1. Introduction

The ability to create 3D structures at micrometer and smaller scales, coupled with the ability to move and control minute volumes of fluid within these structures, has enabled the development of the microfluidics in a wide range of fields, such as life sciences, chemistry and medicine. Comprehensive overviews of microfluidics applications using lab-on-a-chip systems are given by several authors [1–3].

Initially, the majority of the microfluidic work was carried out in devices fabricated in glass and silicon [4–8]. However, fabrication of microfluidic devices in polymers has clear advantages over these more conventional substrate materials [9]. Polymers are biocompatible, cheap, disposable and easy to process, and can be imprinted to replicate structures in a low cost, fast and high throughput process. Polymers also have a wide range of physical and chemical characteristics with different functionalities suitable for a variety of applications. For these reasons, polymers are becoming an increasingly popular material for fabricating microfluidic devices. A number of techniques have been used for fabrication of plastic microfluidic devices including soft lithography [10, 11], laser ablation [12], hot embossing or imprinting [13–15], injection molding [16] and x-ray photolithography [17].

In this paper, for the first time, a novel method to fabricate microfluidic devices by proton beam writing (PBW) is reported. PBW uses an accelerated focused beam of MeV protons to irradiate a positive resist such as poly(methylmethacrylate) (PMMA) or a negative resist such as SU-8. This technique is the proton beam analog to direct-write, electron beam lithography. The main advantage of using protons as opposed to electrons is that protons have a well-defined range and straight path in a polymer [18], and as a consequence, 3D structures with vertical, smooth sidewalls, high aspect ratios and well-defined depths [19] ($\pm 1\%$ depth control using 2 MeV protons) can be fabricated. Recently, PBW has indicated a high resolution of 20 nm that presents the technique as one of the candidates for next generation lithography (NGL) [20]. These features are advantageous in micro analytical applications when optical detection methods are used, since larger optical paths provide for higher sensitivity. This is critical in practical analytical applications to obtain reproducible and repeatable data from device to device. These characteristics make PBW very useful for applications which require a 3D capability, for example, when fabricating photonic structures [21]. PBW also has the capability of modifying surface chemistry through atomic displacement, and this aspect has been used in combination with electrochemical etching to pattern 3D structures in silicon and to produce areas with light emitting characteristics on the surface of silicon [22]. The unique characteristics of PBW can also be used to integrate optical and optoelectronic components into microfluidic structures and this technology offers great potential for fabricating integrated lab-on-a-chip devices. However, as yet, an automated, user-friendly, p-beam writer is not commercially available, although a prototype system has been constructed in CIBA (Center for Ion Beam Applications) and a compact system has been designed. One of the niche areas of application for PBW is the fabrication of 3D micro- and nanostamps for nanoimprint lithography, in order

to produce commercial quantities of polymeric devices. We have developed a fabrication process for high-quality stamps with a combination of PBW and nickel electroplating [23]. PBW, because of its 3D capability, is also a technique ideally suited to the fabrication of microchannels and microfluidic devices.

Electrokinetic pumping is considered as the method of choice for fluidic transport in microchannels [24–28], which is widely used because it has important advantages over other fluid transport mechanisms, most importantly, a flat velocity profile, a non-mechanical pulsation free flow, ease of operation and integration, and the capability of parallel analytical processing. Electrokinetic pumping depends on the surface charge of the channels, which is an intrinsic characteristic of the contact chemistry between the fluid and the channel material. Surface charge arises from ionization of functional groups at the surface produced from the opposing forces of electrical repulsion, and chemical attraction (van der Waals force) [29]. At relatively high pH buffers with excess of OH^- group, these interactions result in ionization of surface groups; in materials with no ionizable surface groups, charge can arise by adsorption of charges from the polar medium [30–32]. The produced surface charge spontaneously forms a thin ionic layer adjacent to the walls called the electric double layer (EDL). The potential drop associated with the outer diffuse portion of the double layer (slip plane), known as the Gouy–Chapman layer, is called the zeta potential and effectively depends on the chemical and physical characteristics of the surface of the polymer and solution in contact. An applied external electric field along the channel exerts a force on the diffuse ions of the EDL and draws the layer toward the electrode with the opposite polarity. This creates a flow of fluid near to the walls of the channel. The flow is transferred through viscous drag to the rest of the fluid which is electrically neutral, thereby resulting in a bulk flow of fluid. Two pertinent parts of the electrokinetic effect are electroosmosis and electrophoresis. Electroosmosis flow (EOF) concerns the bulk flow of fluid and electrophoresis (EP) concerns the motion of electric-field-driven, charged species suspended in the solution.

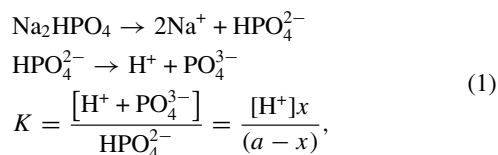
In this paper, we present the fabrication of microfluidic channels in PMMA by direct PBW and the experimental characterization of their electrokinetic characteristics using the methods of current monitoring and particle image velocimetry. A numerical simulation is presented for the particular experimental parameters used in this work, and the experimental and theoretical results are compared.

2. Theory

Following the pioneering work of Burgreen and Nakache [33], the first formulation of electrokinetic flow in micron-size capillaries was presented by Rice and Whitehead [34]. Hildreth has conducted a numerical study for electrokinetic flow in slit channels [35]. Patankar and Hu [24] developed a 3D numerical method for the electrokinetic flow in rectangular microchannels. Santiago *et al* [25] studied electrokinetic flows in microchannels in the presence of external inertial and pressure forces. Dongli *et al* [26, 36] studied electrokinetic phenomena in microchannels under different fluidic conditions, arbitrary geometries and arbitrary

distribution of wall charge. Most of these studies were carried out on microchannels fabricated in glass or silicon, whereas for polymeric microchannels there are only few works with experimental and numerical calculations reported [37–41].

In this section, we formulate the theory that we use to simulate and compare the electrokinetic flow in the microchannels with our experimental results. A numerical, finite-difference scheme using the Gauss–Seidel iterative method with successive overrelaxation criterion was employed to converge the iterations quickly. More details of the simulation method are explained elsewhere [26]. The fluid is assumed to be Newtonian with laminar flow and is acted on by only the external electric force. The flow velocity is determined by first solving the Laplace equation to obtain the electric charge density and the electric field strength inside the microchannel, and by inserting these quantities into the Navier–Stokes equations for the fluid motion. The simulation was carried out for a 20 mM phosphate solution. Phosphate dissociation reactions are as follows:



where K is the dissociation constant, and a is the concentration of the phosphate solution (20 mM). The second reaction can be ignored due to its small equilibrium constant. Most of the ions in the solution are in the form of Na^+ and HPO_4^{2-} . Hence, the net charge density per unit volume is given by

$$\begin{aligned} \rho_e(r) &= e(z_{\text{Na}}n_{\text{Na}} + z_{\text{HPO}_4^{2-}}n_{\text{HPO}_4^{2-}} - n_{\text{HPO}_4^{2-}}) \\ &= e((+1)2n_0 e^{-(e\psi/k_B T)} + (-2)n_0 e^{(2e\psi/k_B T)}) \\ &= -2en_0(e^{(2e\psi/k_B T)} - e^{-(e\psi/k_B T)}). \end{aligned} \quad (2)$$

Substituting the above expression into Poisson's equation [27] we obtain

$$\frac{\partial^2 \psi}{\partial y^2} + \frac{\partial^2 \psi}{\partial z^2} = \frac{2en_0}{\epsilon} (e^{(2e\psi/k_B T)} - e^{-(e\psi/k_B T)}). \quad (3)$$

Substituting the charge density $\rho_e(r)$ into Navier–Stokes equation leads to the momentum differential equation

$$\eta \left(\frac{\partial^2 u}{\partial y^2} + \frac{\partial^2 u}{\partial z^2} \right) = \frac{2en_0}{\epsilon} (e^{(2e\psi/k_B T)} - e^{-(e\psi/k_B T)}) E_x. \quad (4)$$

3. Experimental section

3.1. Microchannel fabrication using PBW

The lithographic patterning was carried out using the PBW facility at the National University of Singapore [42]. Two beam-scanning methods were used to fabricate the PMMA microchannels in this study. The first method utilizes a magnetic scan system, which uses a set of magnetic scan coils to deflect the proton beam over a total area no greater than $2 \times 2 \text{ mm}^2$. Larger structures can be fabricated by combining magnetic beam scanning and scanning the sample stage at a constant speed. Using this method, structures over areas as large as $2.5 \times 2.5 \text{ cm}^2$ can be fabricated. The typical irradiation parameters used in the patterning experiments are

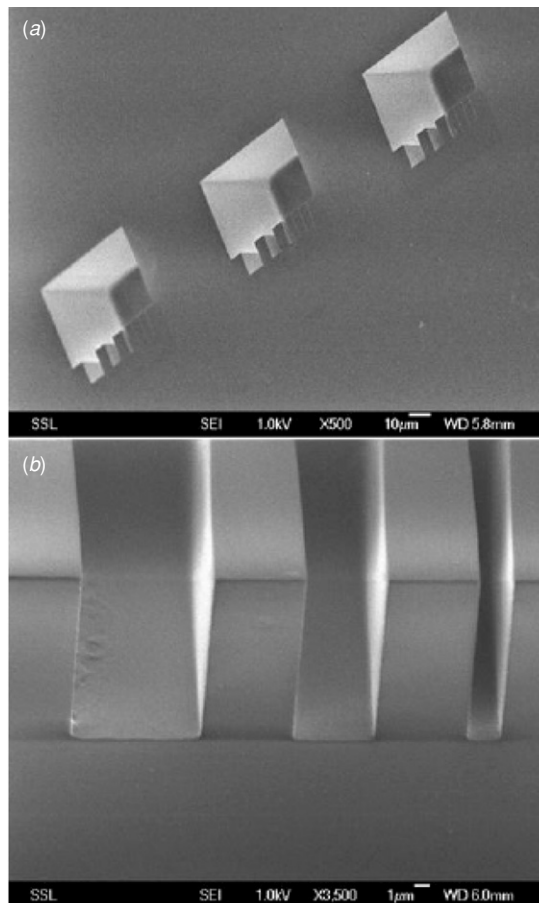


Figure 1. (a) A scanning electron micrograph (SEM) of test microchannels fabricated in PMMA solid sheets irradiated with a 2 MeV proton beam. (b) A close view of the SEM image of microchannels with $60 \mu\text{m}$ depth and widths between $10 \mu\text{m}$ and 400 nm , connected to $10 \mu\text{m}^2$ reservoirs.

a magnetic scan speed of 1 mm s^{-1} , and a beam fluence of $\sim 10^{14}$ protons cm^{-2} . This corresponds to a beam current of 50 pA or less, with a beam size below $1 \times 1 \mu\text{m}^2$ or less (beam sizes of down to $35 \times 75 \text{ nm}^2$ have been achieved [43]), at a dose of 80 nC mm^{-2} (1 proton per 2 nm^2). The depth of the channels in thick resist material can be controlled by the energy of the incident beam: for example, the penetration depth for 2 MeV protons and 2 MeV H^{2+} is approximately $63 \mu\text{m}$ and $20 \mu\text{m}$, respectively, in PMMA [44]. After irradiation the latent structures are developed using a GG developer (60% DGMBE (diethyleneglycolmonobutylether), 20% morpholine, 5% ethanolamine, 15% water) for 30 min at 35°C , followed by a rinse in deionized water for 1 h. Figure 1 shows the results of a test study using PBW to fabricate structures and channels in thick resist, showing the precise nature of the fabricated structures at depth in the resist. The substrate material used is a thick piece (2 mm) of PMMA sheet (Röhm GS 233 PMMA, GmbH & Co., Germany) with a high average weight molecular mass $M_w \sim 3 \times 10^6 \text{ g mol}^{-1}$ and 1.19 g cm^{-3} density. PMMA is a positive resist for protons, which means that during fabrication, only the area corresponding to the microchannels needs to be irradiated.

To obtain wider and longer channels, a combination of magnetic scanning and stage scanning was used. A beam

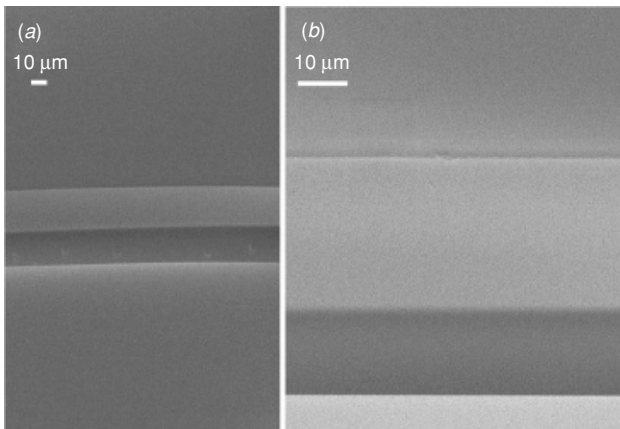


Figure 2. SEM image of a 2 cm long channel in thick PMMA. The stage velocity was $40 \mu\text{m s}^{-1}$ with $1 \times 1 \mu\text{m}^2$ beam spot size.

of 2 MeV protons focused down to a $1 \times 1 \mu\text{m}^2$ spot was magnetically scanned over a length of $50 \mu\text{m}$ in the x -direction, while the stage was driven at a constant speed of $40 \mu\text{m s}^{-1}$ in the y -direction. Figure 2 shows an SEM image of these channels.

3.2. Bonding process

After fabrication of the channels by PBW, the channels must be bonded to avoid fluid evaporation. Channel access is provided via through-hole reservoirs at the termini of the channels. In our case, the through holes were constructed using conventional mechanical drilling from the backside of the chip, and the alignment obtained using an inverted microscope. After the through-hole reservoirs were drilled, the channel was enclosed using a flat section of PMMA with thermal bonding. The substrate containing the microfabricated channel and the flat section of PMMA was sandwiched between two microscope slides under 2 kg cm^{-2} pressure, and heated up to $145 \text{ }^\circ\text{C}$ for 30 min. After bonding, the structures were gradually cooled down to room temperature. Figures 3(a) and (b) show a four-port, T-cross, microchannel device with an inset that depicts the cross section of a sealed microchannel. Our observations indicate that thermal bonding can be achieved successfully for PMMA of similar molecular weights (MWs) and from the same supplier. However, bonding

of different types of PMMAs in terms of MW or purchase from different suppliers proved difficult or unsuccessful in most cases.

3.3. Surface roughness measurement

One of the features of PBW is its ability to produce smooth sidewalls. To determine the surface smoothness of the PBW microchannels, we used atomic force microscopy (AFM). A $50 \times 50 \mu\text{m}^2$ area was irradiated with a 2 MeV proton beam focused to a $800 \times 800 \text{ nm}^2$ beam spot size. The structure was machined over the edge of a 2 mm thick PMMA sheet at 90° to the normal beam-scanning direction in order to provide access to the sidewall of the channel by the AFM (see figure 4). Figure 4(a) shows a typical picture of the patterned areas fabricated at the edge of the substrate. The surface roughness was measured over an area of $2 \times 2 \mu\text{m}^2$ using an AFM in tapping mode and a sidewall roughness of 2.45 nm RMS at different depths was obtained (see figure 4(b)).

3.4. Flow experiments

Flow measurements were performed using a $50 \mu\text{m}$ (width) \times $50 \mu\text{m}$ (depth) \times 2.1 cm (length) bonded PMMA microchannel connected to a 2 mm diameter reservoirs. Large reservoirs were used to ensure a minimal electrolysis effect on the buffer electrolyte, which destabilizes the ionic strength and pH of the solution and, therefore, the measured current. To characterize the electrokinetic behavior of the fabricated microchannels, a series of current-versus-time measurements at different pH values and electric field strengths were conducted. Five standard electrophoretic buffers were used: sodium dihydrogenphosphate (pH 2.50), sodium acetate (pH 5.00), disodium hydrogenphosphate (pH 7.20), tris[(hydroxymethyl)aminomethane hydrochloride] (tris) (pH 8.00) and sodium borate (pH 9.05). The lower conductivity buffers were prepared by diluting an aliquot to 18 mM. Before conducting the tests, the microchannels were conditioned for 10 min with the solution to be tested. To carry out the current-monitoring tests, the microchannel and the fluid reservoir at the cathode side were filled with the 20 mM buffer. The second fluid reservoir on the anode side was filled with the same buffer at a concentration of 18 mM. When an electric field is applied between both reservoirs, the 18 mM buffer flows into the channel and displaces the 20 mM buffer, resulting

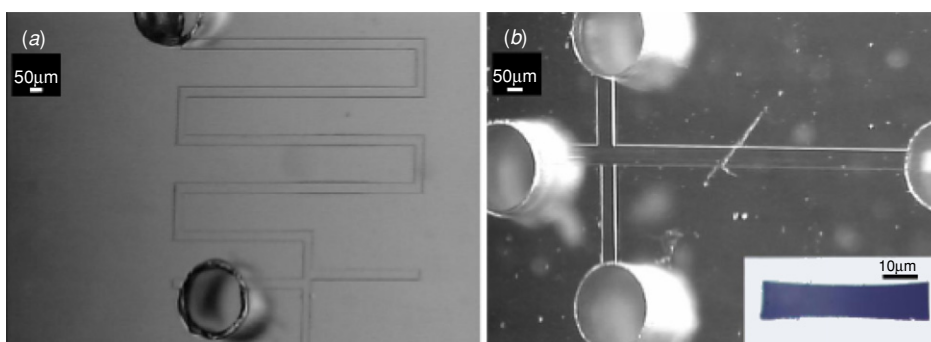


Figure 3. (a) An angled microchannel with 90° turning points (b) A four-port, T-cross, microchannel, both made in PMMA. The inset is an optical micrograph of the cross section of the sealed microchannel.

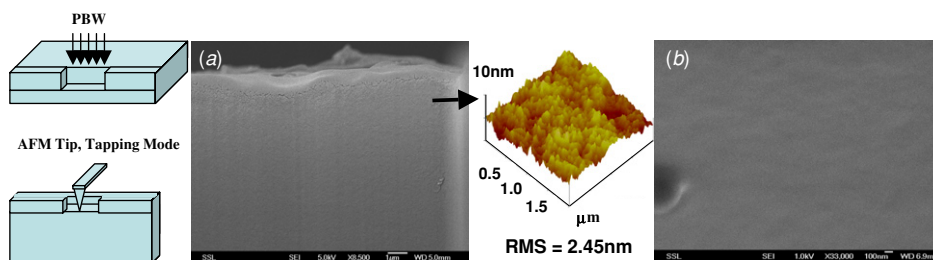


Figure 4. Schematic diagram of the AFM measurement. (a) SEM image on the sidewall of an open PMMA channel fabricated at the edge. AFM image of the selected region in (a), and (b) SEM image of a region where AFM measurements were performed.

(This figure is in colour only in the electronic version)

in a decrease in current signal. When the 18 mM buffer completely filled the channel, the current reached a constant value. The reverse process was also performed by swapping the position of the buffers at the anode and cathode reservoirs and filling the channel and the cathodic reservoir with the low concentration (18 mM) buffer. In this case, the higher concentration buffer (20 mM) flows into the channel and displaces the lower concentration buffer (18 mM) and an increase in current is observed. After the 20 mM buffer fills the channel completely, the current reaches a steady-state value. The tests were performed in triplicate at voltages of 100, 200 and 400 V. The voltage was applied and the current associated with the displacement process was recorded using a Keithley picoammeter and power source Model 487. Data were collected every 1.0 s and recorded as a function of time. The bulk liquid conductivity of the prepared solutions was measured using a high-precision conductivity meter (Mettler Toledo).

3.5. Particle imaging setup

The seed particles used in the experiment had a diameter of 600 nm, with negatively charged sulfate surface groups, chosen to minimize the adherence of the particles to the walls of the channels and to reduce agglomeration. Video images of the particles were taken when a constant particle flow velocity was observed, the video frames taken by focusing the microscope in the middle of a $50 \mu\text{m}$ (width) \times $20 \mu\text{m}$ (depth) \times 2 mm (length) microchannel. The microfluidic system was observed using an Olympus microscope equipped using a $150\times$ magnification, oil-immersion, objective lens with a numerical aperture (NA) of 1.2 and a $200 \mu\text{m}$ working distance (WD). The addition of a $2.5\times$ eyepiece provided a total system magnification of $M = 190 \text{ nm/pixel}$. Particle images were recorded using a Princeton Instruments Micromax cooled interline-transfer, charge-coupled device camera with a 1024×1024 pixel array and 12-bit readout resolution. The measurement depth determined experimentally was $2 \mu\text{m}$, consistent with quantitative depth estimates for particles with the size of $d_p = 0.6 \mu\text{m}$, $\text{NA} = 1.4$, $\lambda_0 = 700 \text{ nm}$ for normal light, $n = 1.515$ (oil) and $\sin \theta = \text{NA}/n$ [45]. The velocity fields in the fluid were calculated by tracking the motion of the microspheres for an applied electric field of 30 V cm^{-1} .

An image processing program, implemented in IDL, a programming language optimized for visual data analysis, has been developed to locate the centroids of the candidate particle position in each frame by identifying local brightness

maxima. An algorithm refines these positions obtained from sequence of frames, discriminating ‘false’ particles, and finally linking the time-resolved particle locations into trajectories. Determining which particle in a given image most likely corresponds to that in the preceding image requires colloidal particles large enough to image with a conventional optical microscope. Colloidal particles at these dimensions typically diffuse through water a distance smaller than their diameters in the video frame interval. Consequently, particles misidentification rarely imposes a practical limit on particle tracking at video frame rates.

4. Results and discussion

4.1. Proton beam writing

When MeV energetic protons penetrate into a low- z material, they transfer energy to the material using two mechanisms: energy transfer to the target nuclei, and to atomic electrons. The dominant energy transfer mechanism is to atomic electrons, which in turn produces many short-range secondary electrons very close to the path of the incident proton beam. In proton/electron scattering, the scattering of protons by atomic electrons is small compared with electron/electron scattering. The protons can, therefore, penetrate deep into the resist while maintaining a straight path, and also while transferring energy. However, as the protons get near to their end of range, the proton/nuclear scattering mechanism becomes more dominant, and therefore toward the end of range the scattering of the protons is increased, and the proton beam undergoes progressively more broadening. For microchannels, this effect is minimal since the size of the channel is comparatively much larger than the resulting end-of-range beam spread.

To investigate the degree of beam spread from the vertical path on the channel walls, we carried out size measurements on 660 nm wide channels imaged by SEM from an open $20 \times 20 \mu\text{m}^2$ square reservoir area that was fabricated at the edge of a PMMA sheet adjacent to the end of the channel (see the inset in figure 5(a)). Figure 5 shows the SEM images of the 660 nm wide and $65 \mu\text{m}$ deep channel. The SEM images indicate the formation of near vertical sidewalls which appear, up to a depth of approximately $5 \mu\text{m}$. At depths greater than $5 \mu\text{m}$, the cross section of the channel increases gradually, and continues increasing until near to the end of range (corresponding to a depth of $60 \mu\text{m}$), where, due to the rapid increase in the nuclear stopping power or

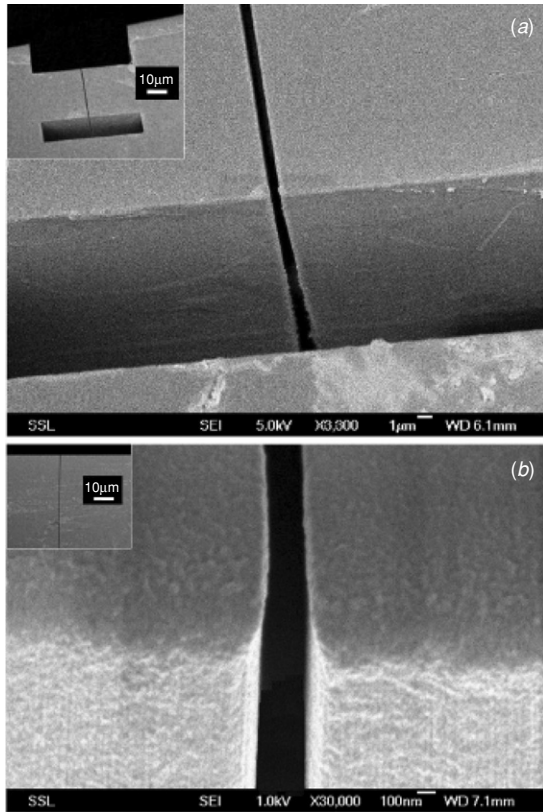


Figure 5. (a) SEM images of a 660 nm channel in thick PMMA connected to $20 \mu\text{m}^2$ reservoirs at the side of an optically polished PMMA sheet. The channel is connected to reservoirs where one of them was positioned at the edge, which after development produced an open space to reveal the channel for SEM imaging in a cross-sectional view. (b) SEM image of a 200 nm channel in PMMA showing straight vertical sidewalls down to $5 \mu\text{m}$ depth with smooth edges and surfaces and high aspect ratio.

energy deposition, the width of the channel increases rapidly. The SEM images of 660 nm channels indicate a lateral increase of the width of the channels of 112 nm at a depth of $12.9 \mu\text{m}$. Factors affecting this lateral spread are the lateral beam spread, the energy of the secondary electrons, the incident angle of the focused beam with respect to vertical direction and any swelling of the polymer during development. Figure 5(b) shows a close view of a 200 nm PMMA channel connected to $20 \times 20 \mu\text{m}^2$ reservoir fabricated by PBW in PMMA. The channel illustrates straight, smooth, vertical sidewalls and edges. The results presented indicate that PBW with 2 MeV energetic protons can be used to fabricate straight-sided and vertical micro- to nano-size fluidic channels at depths up to $5 \mu\text{m}$.

To compare the experimental results with theory, we carried out a Monte Carlo simulation using the computer code SRIM (stopping and range of ions in matter) [44]. Since the average energy transfer per electron collision is relatively small, and many thousands of collisions occur before the proton comes to rest, the results of a Monte Carlo simulation are acceptable. In our simulation, we considered a number of 50 000 protons incident on a PMMA target (lucite $\rho = 1.19 \text{ g cm}^{-3}$) with a layer of thickness starting from $0.1 \mu\text{m}$ and increasing in steps of 0.1 or $0.5 \mu\text{m}$. At every step,

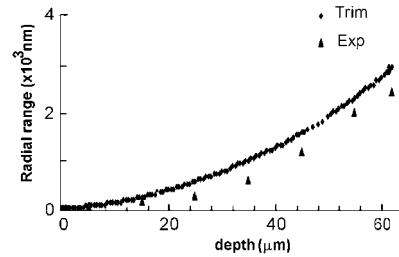


Figure 6. Comparison of experimental and SRIM simulation results of the radial range of a beam of 2 MeV protons incident on PMMA (lucite) target. For experimental measurements we used the lateral increase in the width of the microchannel in figure 5.

we calculated the radial range of the transmitted protons that spread out in the $Y-Z$ plane perpendicular to the incident beam. The radial range was taken as the radius of a circle that covers 90% of the number of transmitted protons. Figure 6 shows the radial range of the beam spread as a function of PMMA depth, using the SRIM calculations and its comparison with experimental results of the width of the channel in figure 5.

4.2. Surface roughness

The wall surface roughness of microfluidic channels is one of the factors affecting fluid flow and heat transfer. It has been experimentally and theoretically proven that the surface roughness becomes important in the low Reynolds number regime. When the size of the channel decreases to a few microns, the surface roughness increases the fluid friction for both pressure-driven flow [46–52] and electrokinetic flow [53]. However, up to now, there has been no experimental published data on the effect of roughness on the EOF or EP in fluidic channels.

The sidewall roughness of 2.45 nm RMS achieved by PBW is a significant improvement by a factor of 2 over other micromachining techniques [54, 55]. We do not anticipate that a small wall roughness has a significant influence on flow characteristics. However, low surface roughness is particularly important in electrophoresis and other analytical applications in order to obtain reproducible results, and reduce undesirable effects such as analyte adsorption.

Since the fabrication of high aspect ratio smooth channels is highly beneficial for sub-micron or nanometer size fluidic channels, PBW represents a method of high potential in this emerging field.

4.3. Current monitoring results

To obtain information on the flow profile and bulk flow rate in the PMMA microchannels fabricated by PBW, digital video microscopy [56], and current monitoring [57] techniques were used. Current monitoring was used to measure the EOF, and video microscopy was used to measure both phenomena EOF and EP jointly. The available techniques for measuring EOF and zeta potential (ζ) for several polymeric materials have been reported in the literature [37–40, 58–61]. Current monitoring is an indirect flow-rate measurement method, which determines the electroosmotic mobility in a

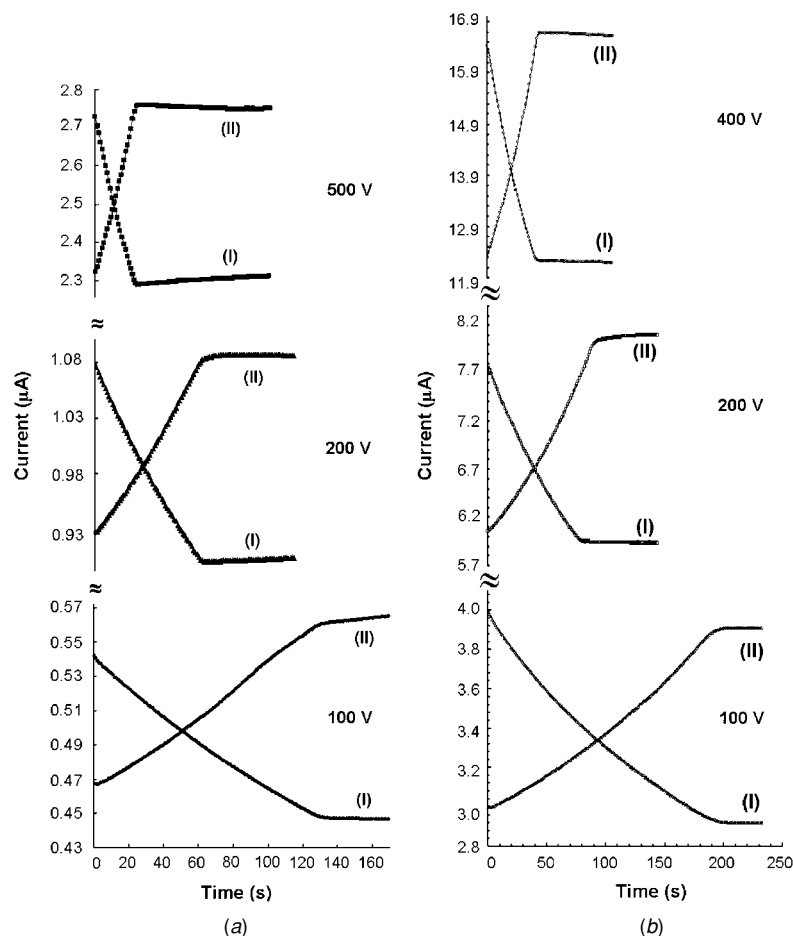


Figure 7. Data obtained from current monitoring experiments in a PMMA microchannel ($50 \mu\text{m} \times 50 \mu\text{m} \times 2.1 \text{ cm}$) using (a) 20/18 mM phosphate (pH 7.20) buffer solution at voltages of 500, 200 and 100 V and (b) 20/18 mM Tris (pH 8.00) at voltages 400, 200 and 100 V. Plot I shows the change in current observed when 18 mM buffer replaces the channel the 20 mM buffer. Plot II shows the current change observed when 20 mM buffer replaces the 18 mM buffer in the channel.

microchannel by measuring the current change associated with the displacement of a buffer electrolyte by the same buffer of lower or higher concentration [57]. The current monitoring experiments were performed when a low concentration buffer replaces the high concentration buffer (figure 7, plot I) and vice versa (figure 7, plot II). Plot I represents the experimentally obtained current–time data when the low concentration buffer (18 mM) is transferred into the channel to replace the high concentration buffer (20 mM). Immediately, after that, by placing higher concentration buffer (20 mM) into both reservoirs, and reapplying the electric field, the higher concentration buffer (20 mM) is transferred into the channel to replace the lower concentration buffer (18 mM)—see plot II. Since the reservoirs were large and the experiments were carried out some time after injection (i.e. when the system had reached a stable condition), the pressure-driven contribution is expected to be minimal.

The EOF mobility at different pHs was calculated using the method described by Ren *et al* [8]. For this purpose, the slope of the transient region of the current time curves obtained was used in the following equation:

$$\text{slope} = \frac{\Delta I}{\Delta t} = \frac{EAC}{\Delta t} \frac{L_{\text{tot}}}{L_{\text{tot}}} = \bar{u}_{\text{ave}} \frac{EA(C_2 - C_1)}{L_{\text{tot}}}, \quad (5)$$

where \bar{u}_{ave} is the average EOF velocity, E is the electric field strength, A is the cross-section area of the microchannel, and $(C_2 - C_1)$ is the bulk conductivity difference between the replaced buffer and the new buffer. Figures 7(a) and (b) illustrate the typical current–time measurements for 20/18 mM of phosphate (pH 7.20) and tris (pH 8.00), respectively.

Figure 8 shows the calculated EOF mobility as a function of pH for the buffers: phosphate (pH 7.20), tris (pH 8.00) and borate (pH 9.05). An increase in μ_{eof} with pH was observed, indicating that the surface charge of the PMMA channels increased with pH. This observation can be attributed to surface ionization of carboxylic groups of the bulk acrylic polymer. The EOF mobility obtained in our experiments was somewhat higher than that reported for other type of PMMA microchannels [37, 40, 58–62]. At the experimental conditions used in this study, we did not detect a measurable EOF with acetate buffer at (pH 5.00) or sodium phosphate at (pH 2.50), indicating that the ionization of the surface was insignificant.

Equation (5), in conjunction with the Helmholtz–Smoluchowski approximation for a thin EDL,

$$u_{\text{eof}} = -\mu_{\text{eof}} E_x \quad (6)$$

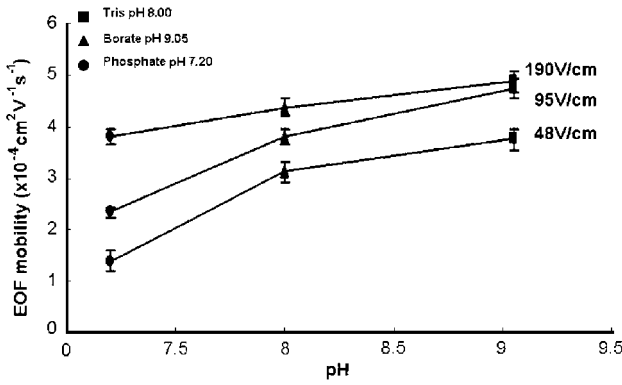


Figure 8. Experimental measured electroosmotic mobility as a function of buffer pH.

Table 1. EOF mobilities for the PMMA microchannel ($50 \times 50 \mu\text{m}^2$ cross section, 2.1 cm long) measured for 20/18 mM borate (pH 9.05), 20/18 mM tris chlorate (pH 8.00) and 20/18 mM phosphate (pH 7.20) buffers.

Buffer	Applied voltage (V)	μ_{eof} ($10^{-4} \text{ cm}^2 \text{ V}^{-1} \text{ s}^{-1}$)	ζ_{eof} (mV)
Borate (pH 8.00)	400	4.9 ± 0.1	68.9 ± 6.9
	200	4.7 ± 0.2	99.9 ± 5.0
	100	3.7 ± 0.3	52.9 ± 4.3
Tris (pH 8.00)	400	4.4 ± 0.1	61.8 ± 0.8
	200	3.8 ± 0.2	53.8 ± 2.6
	100	3.1 ± 0.2	44.1 ± 3.4
Phosphate (pH 7.20)	400	3.8 ± 0.5	53.8 ± 7.0
	200	2.3 ± 0.5	32.9 ± 7.2
	100	1.4 ± 0.2	19.6 ± 3.2

$$\mu_{\text{eof}} = \frac{\varepsilon \zeta_{\text{eof}}}{\eta} \quad (7)$$

was used to obtain the EOF mobility μ_{eof} , and from there the zeta potential (ζ_{eof}) of the channel walls can be calculated.

Table 1 summarizes the calculated EOF mobility and zeta potential (ζ_{eof}) of the PMMA microchannel at voltages of 400, 200 and 100 V with the different buffer pHs. The calculated mobilities and zeta potentials are higher than the measurements reported in the literature [37, 40, 59–62]. In our study, the buffer characteristics are assumed to be similar to the deionized water (dielectric constant of $K = \varepsilon/\varepsilon_0$ vacuum permittivity of $\varepsilon_0 = 8.854 \times 10^{-12} \text{ C}^2 \text{ N}^{-1} \text{ m}^{-2}$, and viscosity of 0.001 N s m^{-2}). It is interesting to note that the zeta potential and the EOF mobility values obtained were not constant with the field applied but increased as voltage was raised.

Figure 9 illustrates the observed trend of the EOF mobility increasing with electric field. This phenomenon is not expected to be the result of temperature effects since relatively low electric fields were used. The phenomenon can be explained on the basis of an increase in surface charge due to an additional polarization at the channel surface arising from the application of voltage. That is to say, the electric field induces an increase in the zeta potential. It is also worth noting that this effect is more apparent at lower pHs where the surface charge due to ionization is expected to be less. The dependence of EOF mobility with the applied field was reported before by Bello and co-workers [63], who provided an

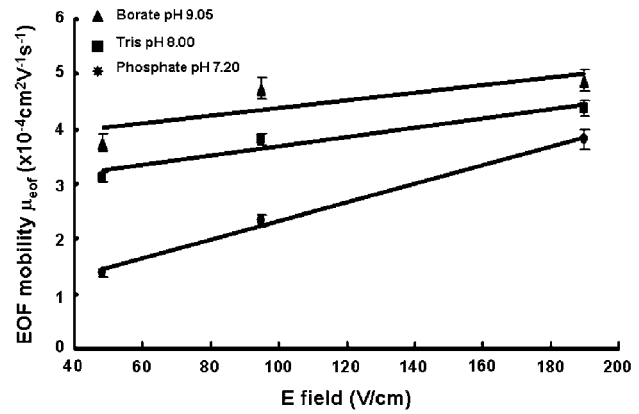


Figure 9. Experimental measured electroosmotic mobility as a function of electric field strength.

experimental and a theoretical model explaining the existence of a radial field in conventional fused silica capillaries.

At sufficiently low electric field strengths the variation of the EOF mobility is small, and hence the plot of velocity versus electric field strength appears linear.

4.4. PIV results

In the field of fluid mechanics, seed particles with micron size dimensions have been used extensively to visualize and quantify fluid flow. An excellent review of particle imaging techniques is presented by several authors [64, 65]. Here, we employed a method of digital video microscopy [66] to image and quantify the fluid velocity profile inside our microchannels.

Figure 10(a) shows a typical optical micrograph of microspheres taken by the particle imaging system. When the colloidal system was stable, the electric field was switched on and the spheres moving along the field direction could be observed on the monitor. In micro-PIV, seed particle size must be small enough to follow the flow without disturbing the flow field, and small enough to avoid clogging the device. At the same time, particles must be large enough to be adequately imaged and to dampen the effects of Brownian motion. Figure 10(b) shows a particle tracking velocity flow field from a series of 70 images for flow in sealed PMMA microchannel. The motion of the particles in the microchannel includes components due to the electrophoretic (EP), electroosmotic (EOF) and Brownian motion (BM).

The normalized histograms of the forward (streamwise) and lateral (spanwise) particle displacements are shown respectively in figures 11(a) and (b). Using a Gaussian fit to each histogram, the standard deviations for the direct and lateral velocities are measured to be $12.5 \mu\text{m s}^{-1}$ and $5.5 \mu\text{m s}^{-1}$, respectively. In the streamwise direction, the variation is due to Brownian motion and differences in particle electrophoretic mobility. The mobility obtained from figure 11(a) represents the total mobility, which is the sum of the electrophoretic mobility and the electroosmotic mobility. Thus, the mean electrophoretic mobility of the particles is obtained by subtracting the electroosmotic mobility obtained by the current monitoring method for similar buffer solution from the total mobility. From figure 11(a), the mean

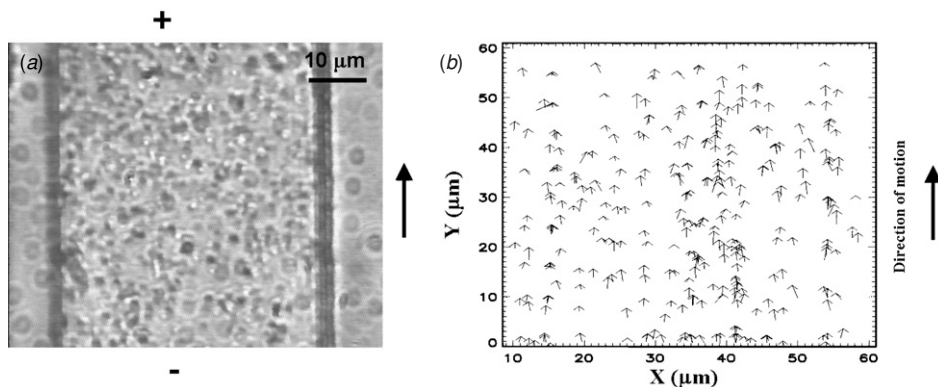


Figure 10. (a) Digital video microscopy of 600 nm polystyrene microspheres (molecular probes) injected into a sealed microfluidic channel. The spheres moved along the length of the channel under a 30 V cm^{-1} externally applied electric field. The mobility of the microspheres was measured by tracking the displacement paths of the moving particles using processed, successively taken optical images. (b) The vectors display the particle tracking of individual spheres measured from 70 consecutive images. The time interval between consecutive frames was 40 ms and the velocity of every particle was averaged over ten frames.

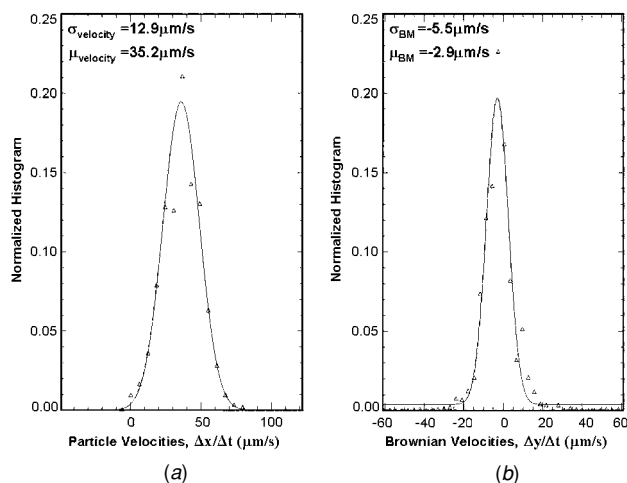


Figure 11. Normalized histogram of electrokinetic velocities for 600 nm particles in PMMA microchannels in the (a) streamwise direction and (b) spanwise or lateral direction. The particle velocities in the streamwise direction are the sum of the electrophoretic and electroosmotic components. The velocities over the measured time interval are plotted on the abscissa.

electrophoretic mobility is $-0.23 \times 10^{-4} \text{ cm}^2 \text{ V}^{-1} \text{ s}^{-1}$ showing a standard deviation of $0.38 \times 10^{-4} \text{ cm}^2 \text{ V}^{-1} \text{ s}^{-1}$.

We also characterized the diffusion constant to reveal how much the microspheres were laterally dispersed when traveling a given distance, as distinct from the lateral spread over a given time. The particle diffusion constant, D , can be estimated from the Einstein diffusion equation

$$\Delta x = (2D\tau)^{1/2}, \quad (8)$$

where Δx is the root-mean-square distance traversed by a molecule during the time interval τ with diffusion coefficient D . Δx is the variance of the Gaussian fit to the lateral (Brownian) velocity (figure 11(b)), which yields a value of $D = 0.61 \times 10^{-12} \text{ m}^2 \text{ s}^{-1}$ for the particle diffusion constant. This value can be compared with the value obtained from the Stokes–Einstein correlation

$$D = \frac{k_B T}{3\pi\eta d_p}, \quad (9)$$

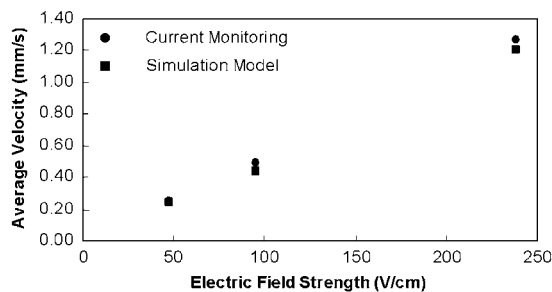


Figure 12. Comparison of the experimental average EOF velocities determined by the current monitoring experiments and theoretical average velocities obtained by the numerical simulation model for 20 mM phosphate (pH 7.20) buffer in the $50 \mu\text{m} \times 50 \mu\text{m} \times 2.1 \text{ cm}$ microchannel.

which yields a value of $0.71 \times 10^{-12} \text{ m}^2 \text{ s}^{-1}$ for $d_p = 600 \text{ nm}$ microspheres immersed in a dilute buffer solution with a viscosity near to the dynamic viscosity of water, $\eta = 0.001 \text{ N s m}^{-2}$ at room temperature.

The slightly smaller experimental value compared with theory has also been reported before [60] and explained as being caused by a decrease in friction between the electrohydrodynamic (EHD) flow and the spheres; the electrokinetic force therefore moves the spheres faster which leads to a reduction in the diffusion constant and hence less dispersion in a given distance.

4.5. Numerical simulation results

Simulations were carried out using the physical and chemical characteristics of deionized water as the fluid: a room temperature ($T = 25 \text{ }^\circ\text{C}$), a phosphate solution with an ionic number density of $n_0 = 1.2 \times 10^{25} \text{ particles m}^{-3}$ in the bulk solution, and an electrolyte concentration of $C = 20 \text{ mM}$, zeta potential values of $\zeta^* = 2.1, 1.3$ and 0.8 , which were measured by current monitoring, $E_x^* = 6.8 \times 10^3, 6.2 \times 10^3, 5.1 \times 10^3$, and double layer thickness parameter of $\kappa^{-1} \sim 2 \text{ nm}$ for a channel with hydraulic diameter of $D_h = 100 \mu\text{m}$. Figure 12 shows the comparison of the average velocity for a 20 mM phosphate buffer solution, according to the numerical

model prediction and the experimental results. The results show a good agreement at lower electric fields and small deviations at higher electric fields. The small deviation at larger electric field strengths could be due to joule heating and surface charging that arises from the application of higher voltages. This results in an increase of mobility and therefore the EOF velocity. The consistency of the calculated bulk velocity and the experimental values confirms the assumption made for the charge density (equation (2)).

5. Conclusion

In conclusion, we have demonstrated the high potential of PBW for the fabrication of microfluidic and nanofluidic channels with precise dimensions, high aspect ratio and high smoothness. We have characterized the electrokinetic flow in the fabricated PMMA microfluidic channels using current monitoring and digital video microscopy techniques. The current monitoring measurements were highly reproducible. The EOF was calculated from the slope of the transient region of the current–time curves. The magnitude of the EOF was somewhat higher than previously reported and dependent on the pH of the buffer electrolyte. A dependence of the EOF mobility with the applied electric field was also observed and this effect was explained in terms of induced zeta potential arising from a polarization effect at the channel surface with applied voltage. Particle tracking experiments showed that the velocity profile of the electrokinetic flow inside the channels was laminar and flat. A numerical model was developed to predict the bulk electroosmotic flow for phosphate buffer solution. The model showed good agreement with the measured electroosmotic mobilities.

References

- Reyes D R, Iossifidis D, Auroux P A and Manz A 2002 Micro total analysis systems: 1. Introduction, theory, and technology *Anal. Chem.* **74** 2623–36
- Reyes D R, Iossifidis D, Auroux P A and Manz A 2002 Micro total analysis systems: 2. Analytical standard operations and applications *Anal. Chem.* **74** 2637–52
- Mijatovic D, Eijkel J C T and van den Berg A 2005 Technologies for nanofluidic systems: top-down vs. bottom-up a review *Lab. Chip* **5** 492–500
- Harrison D J, Fluri K, Seiler K, Fan Z, Effenhauser C S and Manz A 1993 Micromachining a miniaturized capillary electrophoresis-based chemical analysis system on a chip *Science* **261** 895–7
- Chiem N H and Harrison D J 1998 Monoclonal antibody binding affinity determined by microchip-based capillary electrophoresis *Electrophoresis* **19** 3040–4
- Chou H P, Spence C, Scherer A and Quake S 1999 A microfabricated device for sizing and sorting DNA molecules *Natl Acad. Sci. USA* **96** 11–3
- Lagally E T, Medintz I and Mathies R A 2001 Single-molecule dna amplification and analysis in an integrated microfluidic device *Anal. Chem.* **73** 565–70
- Ren L, Escobedo-Canseco C and Li D 2002 A new method of evaluating the average electroosmotic velocity in microchannels *J. Colloid Interface Sci.* **250** 238–42
- Simmons B A, McGraw G J, Davalos R V, Fiechtner G J, Fintschenko Y and Cummings E B 2006 The development of polymeric devices as dielectrophoretic separators and concentrators *MRS Bull.* **31** 120–4
- Whitesides G M, Ostuni E, Takayama S, Jiang X and Inngber D E 2001 Dna size separation using artificially nanostructured matrix *Annu. Rev. Biomed. Eng.* **3** 335–73
- Reyes D R, Iossifidis D, Auroux P A and Manz A 2002 *Anal. Chem.* **74** 2623
- Quake S R and Scherer A 2000 From micro to nanofabrication with soft materials *Science* **290** 1536–40
- Roberts M A, Rossier J S, Bercier P and Girault H 1997 *Anal. Chem.* **69** 2035
- Martynova L, Locascio L E, Gaitan M, Kramer G W, Christensen R G and Mac-Crehan W A 1997 Fabrication of plastic microfluidic channels by imprinting methods *Anal. Chem.* **69** 4783–9
- Becker H, Dietz W and van den Berg A 1998 Microfluidic manifolds by polymer hot embossing for micro-TAS applications *Micro Total Analysis Systems* ed P Dannberg and D J Harrison (Dordrecht: Kluwer)
- McCormick R M, Nelson R J, Alonson-Amigo M G, Benvegna D J and Hooper H H 1997 Microchannel electrophoretic separations of dna in injection-molded plastic substrates *Anal. Chem.* **69** 2626–30
- Renaud P, van Lintel H, Heuschkel M and van den Berg A 1998 *Micro Total Analysis Systems* ed L Guerin and D J Harrison (Dordrecht: Kluwer)
- van Kan J A, Sum T C, Osipowicz T and Watt F 2000 Sub 100 nm proton beam micromachining: theoretical calculations on resolution limits *Nucl. Instrum. Methods B* **161** 366–70
- van Kan J A, Bettiol A A, Ansari K, Shao P and Watt F 2004 Improvement in proton beam writing at the nano scale *Proc. IEEE* pp 673–6
- van Kan J A, Bettiol A A and Watt F 2006 Proton beam writing of three-dimensional nanostructures in hydrogen silsesquioxane *Nano Lett.* **6** 579–82
- Bettiol A A, Sum T C, Cheong F C, Sow C H, Rao S V, van Kan J A, Teo E J, Ansari K and Watt F 2005 A progress review of proton beam writing applications in microphotronics *Nucl. Instrum. Methods B* **231** 364–71
- Breese M B H, Teo E J, Mangaiyarkarasi D, Champeaux F, Bettiol A A and Blackwood D 2005 Proton beam writing of microstructures in silicon *Nucl. Instrum. Methods B* **231** 357–63
- Ansari K, van Kan J A, Bettiol A A and Watt F 2004 Fabrication of high aspect ratio 100 nm metallic stamps for nanoimprint lithography using proton beam writing *Appl. Phys. Lett.* **85** 476–8
- Patankar N A and Hu H H 1998 Numerical simulation of electroosmotic flow *Anal. Chem.* **70** 1870–81
- Santiago J G 2001 Electroosmotic flows in microchannels with finite inertial and pressure forces *Anal. Chem.* **73** 2353–65
- Yang C, Li D and Masliyah J H 1998 Modeling forced liquid convection in rectangular microchannels with electrokinetic effects *Int. J. Heat Mass Transfer* **41** 4229–49
- Arulanandam S and Li D 2000 Liquid transport in rectangular microchannels by electroosmotic pumping *Colloids Surf. A* **161** 89102
- Morf W E, Guenat O T and de Rooij N F 2001 Partial electroosmotic pumping in complex capillary systems: Part 1. Principles and general theoretical approach *Sensors Actuators B* **72** 266–72
- Lyklema J 2003 Electrokinetics after Smoluchowski *Colloids Surf. A* **222** 5–14
- Ni H and Amme R C 2003 Ion redistribution in an electric double layer *J. Colloid Interface Sci.* **260** 344–8
- Kirby B J and Hasselbrink E F Jr 2004 Zeta potential of microfluidic substrates: 1. Theory, experimental techniques, and effects on separations *Electrophoresis* **25** 187–202
- Zembala M 2004 Electrokinetics of heterogeneous interfaces *Adv. Colloid Interface Sci.* **112** 59–2
- Burgreen D and Nakache F R 1964 Electrokinetic flow in ultrafine capillary slits *J. Phys. Chem.* **68** 1084–91

- [34] Rice C L and Whitehead R 1965 Electrokinetic flow in a narrow cylindrical capillary *J. Phys. Chem.* **69** 4017–24
- [35] Hildreth D 1970 Electrokinetic flow in fine capillary channels *J. Phys. Chem.* **74** 2006–15
- [36] Xuan X and Li D 2005 Electroosmotic flow in microchannels with arbitrary geometry and arbitrary distribution of wall charge *J. Colloid Interface Sci.* **289** 291–303
- [37] Kirby B J and Hasselbrink E F Jr 2004 Zeta potential of microfluidic substrates: 2. Data for polymers *Electrophoresis* **25** 203–13
- [38] Mela P, van den Berg A, Fintschenko Y, Cummings E B, Simmons B A and Kirby B J 2005 The zeta potential of cyclo-olefin polymer microchannels and its effects on insulative (electrodeless) dielectrophoresis particle trapping devices *Electrophoresis* **26** 1792–9
- [39] Skulan A J, Barrett L M, Singh A K, Cummings E B and Fiechtner G J 2005 Fabrication and analysis of spatially uniform field electrokinetic flow devices: theory and experiment *Anal. Chem.* **77** 6790–7
- [40] Ross D, Johnson T J and Locascio L E 2001 Imaging of electroosmotic flow in plastic microchannels *Anal. Chem.* **73** 2509–15
- [41] Sinton D A and Li D 2003 Microfluidic velocimetry with near-wall resolution *Int. J. Therm. Sci.* **42** 847–55
- [42] Watt F, van Kan J A, Rajta I, Bettiol A A, Choo T F, Breese M B H and Osipowicz T 2003 The national university of Singapore high energy ion nano-probe facility: performance tests *Nucl. Instrum. Methods B* **210** 14–20
- [43] van Kan J A, Bettiol A A and Watt F 2003 Three-dimensional nanolithography using proton beam writing *Appl. Phys. Lett.* **83** 1629–31
- [44] Ziegler J F 2004 Srim-2003 *Nucl. Instrum. Methods B* **219–220** 1027–36 website: www.srim.org
- [45] Meinhart C D, Wereley S T and Gray M H B 2000 Volume illumination for two-dimensional particle image velocimetry *Meas. Sci. Technol.* **11** 809–14
- [46] Brutin D and Tadrist L 2003 Experimental friction factor of a liquid flow in microtubes *Phys. Fluids* **15** 653–61
- [47] Kandlikar S G, Joshi S and Tian S 2003 Effect of surface roughness on heat transfer and fluid flow characteristics at low Reynolds numbers in small diameter tubes *Heat Transfer Eng.* **24** 4–16
- [48] Koo J and Kleinstreuer C 2003 Liquid flow in microchannels: experimental observations and computational analyses of microfluidics effects *J. Micromech. Microeng.* **13** 568–79
- [49] Koo J and Kleinstreuer C 2003 Experimental friction factor of a liquid flow in microtubes *Phys. Fluids* **15** 653–61
- [50] Koo J and Kleinstreuer C 2004 Modeling of surface-fluid electrokinetic coupling on the laminar flow friction factor in microtubes *Microscale Thermophys. Eng.* **9** 33–48
- [51] Wu H Y and Cheng P 2003 An experimental study of convective heat transfer in silicon microchannels with different conditions *Int. J. Heat Mass Transfer* **46** 2547–56
- [52] Baviere R, Ayela F, Le Person S and Favre-Marinet M 2005 Experimental characterization of water flow through smooth rectangular microchannels *Phys. Fluids* **17** 098105
- [53] Hu Y, Werner C and Li D 2003 Electrokinetic transport through rough microchannels *Anal. Chem.* **75** 5747–58
- [54] Chabloz M, Sakai Y, Matsuura T and Tsutsumi K 2000 Improvement of sidewall roughness in deep silicon etching *Microsyst. Technol.* **6** 86–9
- [55] Studer V, Pepin A and Chen Y 2002 Nanoembossing of thermoplastic polymers for microfluidic applications *Appl. Phys. Lett.* **80** 3614–6
- [56] Crocker J C and Grier D G 1996 Methods of digital video microscopy for colloidal studies *J. Colloid Interface Sci.* **179** 298–310
- [57] Huang X, Gordon M J and Zare R N 1988 Current-monitoring method for measuring the electroosmotic flow rate in capillary zone electrophoresis *Anal. Chem.* **60** 1837–8
- [58] Gaudioso J and Craighead H G 2002 Characterizing electroosmotic flow in microfluidic devices *J. Chromatogr. A* **971** 249–53
- [59] Locascio L E, Perso C E and Lee C S 1999 Measurement of electroosmotic flow in plastic imprinted microfluid devices and the effect of protein adsorption on flow rate *J. Chromatogr. A* **857** 275–84
- [60] Pittman J L, Henry C S and Gilman S D 2003 Experimental studies of electroosmotic flow dynamics in microfabricated devices during current monitoring experiments *Anal. Chem.* **75** 361–70
- [61] Ross D and Locascio L E 2003 Effect of caged fluorescent dye on the electroosmotic mobility in microchannels *Anal. Chem.* **75** 1218–20
- [62] Devasenathipathy S, Santiago J G and Takehara K 2002 Particle tracking techniques for electrokinetic microchannel flows *Anal. Chem.* **74** 3704–13
- [63] Bello M S, Capelli L and Righetti P G 1994 Dependence of the electroosmotic mobility on the applied electric field and its reproducibility in capillary electrophoresis *J. Chromatogr. A* **684** 311–22
- [64] Adrian R J 1991 *Annu. Rev. Fluid Mech.* **23** 261
- [65] Sinton D 2004 Microscale flow visualization *Microfluid Nanofluid* **1** 2–21
- [66] Crocker J C and Grier D G 1996 Methods of digital video microscopy for colloidal studies *J. Colloid Interface Sci.* **179** 298–310